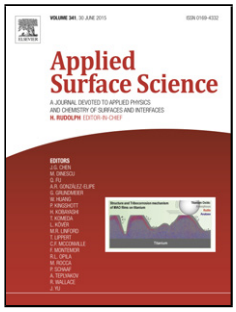

Title: Optimization of $NiFe_2O_4$/rGO composite electrode for lithium-ion batteries

Authors: Chen Li, Xia Wang, Shandong Li, Qiang Li, Jie Xu, Xiaomin Liu, Changkun Liu, Yuanhong Xu, Jingquan Liu, Hongliang Li, Peizhi Guo, Xiu Song Zhao

PII: S0169-4332(17)31110-8
DOI: http://dx.doi.org/doi:10.1016/j.apsusc.2017.04.093
Reference: APSUSC 35774

To appear in: *APSUSC*

Received date: 7-2-2017
Revised date: 10-4-2017
Accepted date: 12-4-2017

Please cite this article as: Chen Li, Xia Wang, Shandong Li, Qiang Li, Jie Xu, Xiaomin Liu, Changkun Liu, Yuanhong Xu, Jingquan Liu, Hongliang Li, Peizhi Guo, Xiu Song Zhao, Optimization of NiFe2O4/rGO composite electrode for lithium-ion batteries, Applied Surface Sciencehttp://dx.doi.org/10.1016/j.apsusc.2017.04.093

Optimization of $NiFe_2O_4$/rGO composite electrode for lithium-ion batteries

Chen Li[a], Xia Wang[a], Shandong Li[a,*], Qiang Li[a], Jie Xu[a], XiaominLiu[a], Changkun Liu[a], Yuanhong Xu[b], Jingquan Liu[b], Hongliang Li[b], Peizhi Guo[b], and Xiu Song Zhao[b,c]

[a]*College of Physics, Key Laboratory of Photonics Materials and Technology in Universities of Shandong, and Laboratory of Fiber Materials and Modern Textile, the Growing Base for State Key Laboratory, Qingdao University, Qingdao, 266071, China.*

[b]*Institute of Materials for Energy and Environment, Qingdao University, Qingdao 266071, China*

[c]*School of Chemical Engineering, The University of Queensland, St Lucia, QLD 4072, Australia*

*Corresponding author: Prof./Dr. Shandong Li, email: lishd@qdu.edu.cn.

Graphical abstract

A $NiFe_2O_4$/rGO composite wasfabricated via a hydrothermal-annealing method, in which the mean size of spinel $NiFe_2O_4$ nanoparticles was around 20 nm. The optimized $NiFe_2O_4$/rGO electrode with CMC binder exhibited high reversible capacity, good cycling durability and high-rate capability, whereas the electrode with PVDF binder underwent rapid capacity decay.

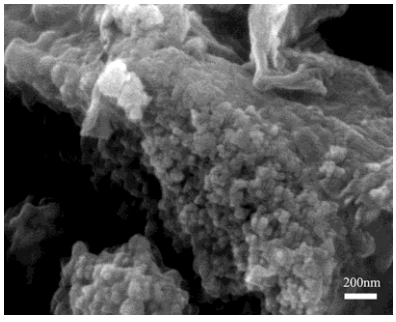

(a)

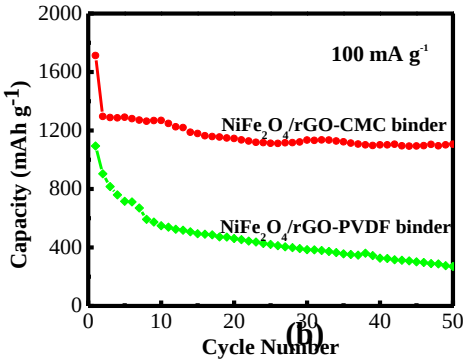

(b)

Highlights

- ● The rGO content in $NiFe_2O_4$/rGO composites was optimized.
- ●Proper choice of binders to improve lithium-storage performance was first compared.
- ●The $NiFe_2O_4$/rGO-CMC binder presented better lithium-storage performance.
- ●The $NiFe_2O_4$/rGO-CMC binder showed a capacity of 1105 $mAhg^{-1}$ after 50 cycles.
- ●The $NiFe_2O_4$/rGO-CMC binder possessed good rate capability of 439 $mAhg^{-1}$ at 5 Ag^{-1}.
-

Abstract

The combination of carbon compositing and the proper choice of binders in one system offer an effective strategy for improving electrode performance for lithium ion batteries (LIBs). Here, we focus on the optimization of reduced graphene oxide content in $NiFe_2O_4$/reduced graphene oxide (abbreviated to $NiFe_2O_4$/rGO) composites and the proper choice of binders to enhance the cycling stability of the $NiFe_2O_4$ electrode. The $NiFe_2O_4$/rGO composites were fabricated by a hydrothermal-annealing method, in which the mean size of spinel $NiFe_2O_4$ nanoparticles was approximately 20 nm. When tested as anode materials for LIBs, the $NiFe_2O_4$/rGO electrodes with carboxymethylcellulose (CMC) binder exhibited excellent lithium-storage performance including high reversible capacity, good cycling durability and high-rate capability. The capacity could be retained as high as 1105 mAh g^{-1} at a current density of 100 mA g^{-1} for over 50 cycles, even cycled at higher current density of 1000 mA g^{-1}, a capacity of 800 mAh g^{-1}can be obtained, whereas the electrode with the polyvinylidene fluoride (PVDF) binder suffered from rapid capacity decay under the same test conditions. As a result, the $NiFe_2O_4$/rGO composites with CMC binder electrode in this work are promising as anodes for high-

performance LIBs, resulting from the synergistic effect of optimal graphene content and proper choice of binder.

Keywords: Lithium ion batteries; anode materials; $NiFe_2O_4$; graphene; binders

1.Introduction

Lithium-ion batteries with distinct merits including long cycling stability, no memory effects, large energy density and environmental friendly have been extensively applied in portable electronic devices and electric vehicles [1]. However, the energy density of the current commercial LIBs is relatively low due to the utilization of graphite anode, which has a theoretical capacity of 372 mAh g^{-1}. It is therefore essential to develop novel electrode materials with high specific capacity, long cycle life and low cost [2].

Transition metal oxides such as Fe_2O_3 [3], Fe_3O_4 [4], Co_3O_4 [5], and NiO [6,7] have been gaining increasing interests on account of their high theoretical capacities, low cost and environment friendly. Recently, mixed transition-metal oxides (MTMOs) such as spinel transition metal oxides have attracted us because it have been shown to exhibit unique electrochemical energy storage properties and there will be a confinement effect between the different metal elements [8-11]. By varying the type and content of metal components in spinel transition metal oxides (AB_2O_4), the working voltage and energy density can be controlled [12]. Among various spinel transition metal oxides, $NiFe_2O_4$ is a promising electrode material for LIBs due to its high theoretical capacities and low toxicity [13]. However, $NiFe_2O_4$ suffers from large

volume variation during charge/discharge, leading to a poor stability against cycling [14].

Two strategies have been shown to be effective in alleviating the large volume change problem, namely using nanostructured electrode materials, such as nanoparticels [3], nanoflowers [15,16] and using composite electrode materials. For the latter strategy, carbon materials such as carbon nanotubes and reduced graphene oxide (rGO) are commonly used to support $NiFe_2O_4$ nanoparticles to provide a buffer layer for the volume change [17]. For example, Zhu *et al.* [18] prepared a $NiFe_2O_4$/rGO hybrid, which was constructed by nanosized $NiFe_2O_4$ crystals confined by few-layered rGO sheets. Originating from the two-dimensional conductive channels and the unique hybrid structure rGO constructed, the hybrid possessed the improved electrochemical performance with a reversible capacity of 560 mAh g^{-1} at a current density of 200 mA g^{-1} after 50 cycles. Besides, hierarchically nanostructured $NiFe_2O_4$/C composites were fabricated by Ding *et al.*[19] through a simple polymer pyrolysis method, retaining a high specific capacity of 780 mAh g^{-1} even after 40 cycles at a current density of 1/8C. The performance improvement can be attributed to carbon as the buffer layer to effectively alleviate the volume change of $NiFe_2O_4$.

Recently some studies have shown that binders also have significant impact on battery characteristics, including cycling stability and irreversible capacity losses. For example, some polymer binders with carboxy groups, including carboxymethyl cellulose (CMC) and sodium alginate (SA), have been successfully used to Fe_2O_3 [20]

or $Co_3V_2O_8$ [21] anodes, respectively, and markedly improved electrode performance has been achieved, which can be originating from their unique properties including sufficient binding of active material, adhesion to current collector, insolubility into electrolyte solution, and chemical/electrochemical stability over a wide potential range. For the electrodes based on metal oxides, especially suffering from the mechanical issues associated with the huge volume expansion upon lithium storage, the selection of an appropriate binder may also be critical for enhancing their electrochemical performance. Li *et al.* [20] investigated the electrochemical performance of α-Fe_2O_3 electrodes using CMC binder, two proprietary binders and polyvinylidene fluoride (PVDF) binder and found that α-Fe_2O_3 electrodes with CMC and two proprietary binders showed better cycling performance than with PVDF binder.

To our knowledge, a dual strategy of $NiFe_2O_4$/rGO composite and proper choice of binders has not been adopted to improve the lithium-storage performance of the $NiFe_2O_4$ electrode. In this work, we fabricated $NiFe_2O_4$/rGO composites successfully via hydrothermal-annealing procedure, in which $NiFe_2O_4$ nanoparticles with a diameter of 20 nm were dispersed on rGO sheets. In addition, the suitable ratio of $NiFe_2O_4$ and rGO in $NiFe_2O_4$/rGO composites and the effect of different binders on the performance of the battery have been also investigated. When tested as an anode material for LIBs, the composites presented excellent cycling stability and high reversible capacity. Meanwhile, the composites with CMC as binder had the

improving rate capability, such as the reversible capacities can keep 1031, 892, 831, 785 and 439 mAh g^{-1} at current densities of 0.4, 0.8, 1.5, 3 and 5 A g^{-1}, respectively.

2. Experimental

2.1 Synthesis of the $NiFe_2O_4$/rGO composites

Graphene oxide (GO) was synthesized from natural flake graphite powder using a modified Hummer's method [22]. The $NiFe_2O_4$/rGO composites were prepared by a hydrothermal-calcination method. Firstly, 0.8 g polyvinylpyrrolidone (PVP) and 0.1 g GO were separately dispersed into 25 mL DI water under ultrasonication, in which PVP was used to control the shape of the $NiFe_2O_4$ grains and further prevent the agglomeration of GO nanosheets. Meanwhile, 0.5 mmol of $Ni(CH_3COO)_2{\cdot}4H_2O$ and 1 mmol $Fe(NO_3)_3{\cdot}9H_2O$ were dispersed into 10 mL DI water. Secondly, the above solutions were slowly mixed with magnetic stirring, followed by adding DI water and 25 wt% ammonia until the pH was 10. And then the mixed suspension was transferred into a Teflon lined stainless steel autoclave and reacted at 180 ^oC for 24 h. After the autoclave was cooled down to room temperature naturally, the black sediments were washed with DI water and ethanol repeatedly to wash away the residual PVP, and dried at 80 ^oC under vacuum for 12 h. Finally, the as-prepared products were annealed at 400 ^oC for 2 h in argon atmosphere to form the $NiFe_2O_4$/rGO composites (named B). For comparison, the composites with different amounts of GO (0.05, 0.15 and 0 g) were also prepared under the same above procedure, which were named A, C and D, respectively.

2.2 Characterization

Powder X-ray diffraction (XRD) patterns were gained using a Rigaku D/Max X-ray diffractometer with Cu Kα radiation at a scan rate of 7° min^{-1} in the 2θ range from 20 to 80°. The thermogravimetric (TG) analysis was performed with a Mettler Toledo TGA-2 thermal gravimetric analyzer from 30 to 800 ^{o}C under an oxygen atmosphere with a heating rate of 10 ^{o}C min^{-1}. The morphologies of the composites were characterized by a JSM-6700F field-emission scanning electron microscopy (FE-SEM) and atomic force microscope/magnetic force microscope (AFM/MFM, Park system, XE7). Raman spectra were collected using a RenishawinVia Plus Micro-Raman spectroscopy system equipped with a 50 mW DPSS laser at 532 nm. X-ray photoelectron spectroscopy (XPS) measurements were carried out on a KRATOS 165 Ultra photoelectron spectrometer with a monochromatic Al-Kα radiation source. All binding energies were calibrated by referencing to C1s (285.0 eV). The specific surface areas were estimated with the Brunauer-Emmett-Teller (BET) method with N_2 adsorption data in the relative pressure range of P/P_0 = 0.3-1.0. The pore size distributions were calculated using the Barrett-Joyner-Halenda (BJH) model applied to the desorption branch of the N_2 isotherms obtained with a Quantachrome Autosorb-IQ-MP/XR surface area and pore analyzer.

2.3 Electrochemical measurements

Electrochemical measurements were carried out at room temperature using a CR2032 coin-type cell with lithium foil as the counter electrode. The working

electrodes were made by mixing 70wt% active materials, 20 wt% acetylene black and 10wt% CMC or PVDF. The resulting slurry was compressed onto Cu foil, which was dried at 80 ^{o}C for 12 h under vacuum. The coin cells were assembled in the glove box filled with purity argon gas. The electrolyte was 1M $LiPF_6$ dissolved in a mixture of EC and DEC (1:1, v:v). The charge-discharge performance was tested between 0.01 and 3 V in the LAND-ct2001A battery testing system at room temperature. Cyclic voltammetry (CV) measurements were carried out on a CHI660E electrochemical workstation, the scan rate of 0.1 mV s^{-1} in a potential range of 0.01-3 V *vs.* Li/Li^{+}. Electrochemical impedance spectroscopy (EIS) data were performed on the same electrochemical workstation by applying a 5 mV amplitude signal from 100 kHz to 0.01 Hz.

3. Results and discussion

Fig. 1

Fig. 1 shows the general synthesis process of $NiFe_2O_4$/rGO composites. At first, graphite oxide (GO) and PVP were sonicated into the DI water to form the uniform suspension of PVP coated GO monolayer [23-27]. And then, with the addition of Ni^{2+} and Fe^{3+} ions into the suspension they would complex with PVP, attach and grow on GO [28, 29]. Meanwhile, when the Ni^{2+} and Fe^{3+} embedded into sheets of GO, PVP could control the growth of the $NiFe_2O_4$ grains and further prevent the agglomeration of GO nanosheets on the reduction process [30]. Finally, ammonia

water were used to regulate pH of the solution, which could contribute to the formation of $NiFe_2O_4$ particles [12].

Fig. 2

In order to investigate the phase composition and crystal structure of the obtained $NiFe_2O_4$/rGO composite, we examined the XRD patterns, shown in Fig. 2a. It can be obviously seen that all the diffraction peaks of $NiFe_2O_4$/rGO composites can be well assigned to the cubic $NiFe_2O_4$ phase (JCPDS 74-2081). Moreover, the broad diffraction peak centered at 26.4° can be observed in the as-prepared samples, which proves the presence of rGO [18]. Besides, no characteristic peaks are observed for impurities such as Fe_2O_3. Additionally, electronic state and composition of the composites under study were detected by XPS (Fig. 2b). The survey spectrum (Fig. 2b) reveals the presence of C, Ni, Fe and O elements, while the high-resolution Ni 2p spectrum presents two characteristic peaks of $NiFe_2O_4$ at 854.2 eV (Fe $2p_{3/2}$) and 871.8 eV (Fe $2p_{3/2}$) [31], associated with a satellite peak of NiO at 861.0 eV (Fig. 2c) [32]. The binding energy centered at 710.0 eV and 723.9 eV, as shown in Fig.2d, can be well assigned the characteristic peaks of Fe $2p_{3/2}$ and Fe $2p_{1/2}$, respectively [31]. The rGO may be identified by the two XPS peaks of C 1s centered at 283.8 eV and 285.1 eV, corresponding to the C-C/C=C and C-O bands, respectively (Fig. 2e) [15]. Therefore, the XPS data well confirm the formation of the $NiFe_2O_4$/rGO composites.

With the aim of further determining the content of rGO in the $NiFe_2O_4$/rGO composites, TG analysis (Fig. 2f) was investigated. It is found that after the loss of coordinated water molecules in the composites (~2%), $NiFe_2O_4$/rGO composites

exhibited pronounced one-step weight loss (11%, 25% and 34% for A, B, C, respectively) when the temperature was in the range of 400-550 ^{o}C, which can be attributed to the combustion of rGO [33]. Therefore, the weight ratio of rGO in the three composites is 11%, 25% and 34% separately. From the results of XRD patterns and TGA of the as-prepared samples, we inferred that the electrical properties of B composite was best, which has been confirmed by subsequent electrochemical measurements. So we carried out a series of analysis and testing on sample B.

Fig. 3

The structure of the $NiFe_2O_4$/rGO composites was further investigated by Raman spectroscopy, and the corresponding spectrum is displayed in Fig. 3a. For rGO and $NiFe_2O_4$/rGO composites, two obvious peaks at 1350 and 1580 cm^{-1} can be assigned to the disordered carbon (D band) and the in-plane vibration of sp^2 carbon atoms of the ordered graphitic carbon (G-band), respectively [17]. What is more, the $NiFe_2O_4$/rGO showed an increased D/G intensity ratio compared with GO, which relates to the disorder crystal structures of GO nanosheets, due to more defects are generated through the in-situ incorporation of metallic oxide into rGO [8, 17, 33, 34]. The specific surface area and pore structure of the $NiFe_2O_4$/rGO composites were measured by N_2 adsorption-desorption isotherms, as illustrated in Fig. 3b, the $NiFe_2O_4$/rGO composites exhibited type IV nitrogen isotherms with a large hysteresis loop in the pressure range of 0.3-1.0 (P/P_0), indicating the existence of mesopores [35]. The pore size distribution curve was calculated by Barrett-Joyner-Halenda (BJH)

method. From the desorption branch (inset of Fig. 3b), the mesoporous $NiFe_2O_4$/rGO composites have a rather wide pore size distribution with an average size of about 20 nm. What is more, the Brunauere Emmette Teller (BET) specific surface area of the $NiFe_2O_4$/rGO composites was calculated to be 78.405 $m^2 g^{-1}$ and the pore volume was measured to be 0.272 $cm^3 g^{-1}$. The results demonstrate that the $NiFe_2O_4$/rGO composites possess large specific surface area and favorable pore size, which is benefited to the diffusion of liquid electrolyte to the bulk materials easier. As a result, high capacity and rate capability will be expected accordingly.

Fig. 4

The morphology of the as-prepared $NiFe_2O_4$/rGO composites (sample B) was characterized by FESEM, presented in Fig. 4. As is observed, the product exhibited sheet structure from low-magnification SEM image (Fig. 4a). The high-magnification SEM image (Fig. 4b, c) depicted that the $NiFe_2O_4$nanoparticles with average size of around 20 nm uniformly grew on the surface or embedded into the rGO, resulting from the prevention of PVP to hinder the agglomeration of rGO and $NiFe_2O_4$ nanoparticles.

Fig. 5

Atomic force microscopy (AFM) images of rGO nanosheets were shown in Fig. 5a and 5b, which provides detailed information about the individual layer of the rGO nanosheets. The cross section analysis in the AFM height images indicate the thickness of the rGO sheets to be 2.04 nm, whereas the thickness of a single layer

rGO was found to be approximately 1 nm [22]. Therefore, the AFM height images confirmed the few layers of rGO. Fig. 5c and 5d show the AFM image of the $NiFe_2O_4$/rGO composites. It can be seen from the morphology and height images that the $NiFe_2O_4$ nanoparticles with about 20 nm were distributed in silicon substrate uniformly, well consistent with the results of the above SEM images.

Fig. 6

The electrochemical performance of the above $NiFe_2O_4$/rGO composites electrode was investigated to verify the great promise of the $NiFe_2O_4$/rGO in lithium storage, including cyclic voltammograms (CV) and galvanostatic discharge-charge measurements. Fig.6a shows the CV curves of the $NiFe_2O_4$/rGO composites from the 1st to the 5th cycle at a scan rate of 0.2 mV s^{-1} in the voltage window of 0.01-3.00 V (*vs.* Li/Li^+). In the first cathodic sweep, a faint peak at around 1.6 V can be observed, which was attributed to the insertion of Li^+ into $NiFe_2O_4$. In addition, a significant peak centered at 0.52 V corresponded to the reduction of Ni^{2+} and Fe^{3+} to Ni^0 and Fe^0, and the irreversible reaction associated with the decomposition of electrolyte and the formation of a solid electrolyte interface (SEI) film [36]. In the subsequent cycles, the main peak shifted to 0.80 V, suggesting that an irreversible phase transformation and structure rearrangement had taken place during the first cycle [37]. This reduction process can be expressed by the following reaction:

$$NiFe_2O_4 + 8Li^+ + 8e^- \rightarrow Ni + 2Fe + 4Li_2O \qquad (1)$$

When it comes to the anodic process, the peak at 1.68 V associated with the oxidation processes of Ni and Fe to NiO and Fe_2O_3 [38]. This oxidation process can be expressed by the following reaction:

$$\mathrm{Ni} + Li_2O \rightarrow NiO + 2Li^+ + 2e^- \quad (2)$$

$$2\mathrm{Fe} + 3Li_2O \rightarrow Fe_2O_3 + 6Li^+ + 6e^- \quad (3)$$

The CV curves are well overlapped from the second cycle to the fifth cycle and peak intensity has no fading, indicating good electrochemical reversibility for the $NiFe_2O_4$/rGO electrodes [39]. Fig. 6b shows galvanostatic discharge-charge voltage profiles of the $NiFe_2O_4$/rGO composites, which was tested at a current density of 100 mA g^{-1}. In the first discharge process, the $NiFe_2O_4$/rGO composites exhibited a short plateau at 1.0 V and a long flat plateau at 0.8 V, agreeing with the results of CV. From the 2nd cycle onwards, the long plateau shifted to about 1.0 V, due to irreversible phase transformation and structural rearrangement [40]. It is also clearly seen that the initial discharge and charge capacities were 1713.1 and 1242.7 mAh g^{-1}, respectively, and hence an initial Columbic efficiency of 72.6% was obtained. The initial irreversible capacity loss probably results from the formation of the solid electrolyte interface (SEI) film and amorphous Li_2O [41].

The cycling performance of the $NiFe_2O_4$/rGO composites was evaluated via the galvanostatic charge/discharge cycling at a current density of 100 mA g^{-1}, shown in Fig. 6c. When CMC was used as a binder for A, B and C composites, the cycling stability of them was excellent. The improving cycling performance may be due to

the formation of hydrogen bond between the CMC binder and $NiFe_2O_4$ nanoparticles [42-44]. In addition, it is obviously found that the B composite with CMC binder presented the best cyclability and highest reversible Li^+ storage capacity during charge/discharge process with a reversible capacity of 1105 mAh g^{-1} after 50 cycles, revealing the most suitable amount of the rGO in the B composites.

Even when the current density was increased to 1 A g^{-1}, the specific capacity of the B composite with CMC binder still maintained at around 840 mAh g^{-1} (Fig. 6d) demonstrating the excellent stability and improved performance. However, compared with CMC binder, the A and B electrodes with PVDF binder suffered from significant capacity fading, both of which exhibited the reversible capacity of only 304-447 mAh g^{-1} at the 50th cycle. Peculiarly, although the reversible capacity of C electrode with PVDF binder was stable, it is maybe caused by the excessive rGO. And because of the relatively fewer $NiFe_2O_4$ particles, the excessive rGO has already agglomerated, so the specific capacity of C electrode is only 600 mAh g^{-1} and it changes unobviously when tested C composite with different binders [45]. In addition, we tested the bare $NiFe_2O_4$ without rGO electrode with CMC binder (D CMC), shown in Fig. 6c, which presented poor cycling stability due to the absence of the rGO as the buffer layer. Therefore, the appropriate rGO content is important for the $NiFe_2O_4$ electrodes.

Fig. 7

Furthermore, the rate capability of the B composite with CMC binder was tested at various current densities from 0.1 to 10 A g^{-1}, shown in Fig. 7a. The reversible capacities of the B with CMC were about 1031, 892, 831, 785 and 439 mAh g^{-1} at current densities of 0.4, 0.8, 1.5, 3 and 5 A g^{-1}, respectively. When the current density was tested in the range of 100-800 mA g^{-1}, the reversible capacities of B electrode with CMC binder faded unapparently, which may be caused by a higher Li^+ diffusion rate in the electrode resulting from a synergistic effect between the reduced graphene oxide and metal oxide particles [34]. All these results proved that the B composite with CMC binder is a very promising anode for LIBs.

In order to further investigate the Li^+ transport kinetics, electrochemical impedance spectra (EIS) analysis was tested for the $NiFe_2O_4$/rGO composites with CMC and PVDF, and the corresponding curves are shown in Fig. 7b. In addition, the correlated equivalent electrical circuit was also inserted in Fig. 7b. The internal resistance (R_e) corresponding to the intercept of the high-frequency semicircle on the Z' axis includes the total resistance of the electrolyte, separator and Li_2O film [17]. The charge transfer resistance (R_{ct}) and constant phase element of the electrode/electrolyte interface including the influence of SEI film (CPE) are correlated with the middle frequency semicircle [42]. The Warburg impedance resulting from the solid-state diffusion of Li^+ into the bulk of the active materials was represented by the straight line at low frequency. As is obviously seen form Fig. 7b, the diameter of the semicircle in the middle frequency area for the $NiFe_2O_4$/rGO electrode with CMC binder is much smaller than that of the electrode with PVDF,

revealing that the charge can transfer more facile in $NiFe_2O_4$/rGO electrode with CMC than with PVDF. The lower R_{ct} of as-prepared electrode with CMC maybe originate from the more robust 3D conducting structure, the more intimate contact of the active materials with current collector and the insolubility into electrolyte of CMC [33]. In addition, the $NiFe_2O_4$/rGO electrode with CMC exhibited larger slope than that of the $NiFe_2O_4$/rGO electrode with PVDF at low frequency, indicating higher Li^+ ion mobility in the solid phase [46]. Moreover, after several cycles, the value of R_{ct} dropped, which may be because the electrode becomes more stable with the soaking and penetrating of electrolyte.

For the evaluation of the adhesion strength between active materials and Cu current collector, we measured the $NiFe_2O_4$/rGO-CMC and $NiFe_2O_4$/rGO-PVDF electrodes by 3M adhesive tape test. In the test, the electrodes were fixed to a fixture with double faced adhesive tape, the pressure sensitive adhesive tape with a 10 N adhesive force were bonding to the electrode absolutely, and then striping adhesive tape as close as possible to a 60 degree angle in 0.5 seconds smoothly. Fig. 7c and d show the results of the testing. It can be seen that the adhesion strength of the $NiFe_2O_4$/rGO-CMC electrode was stronger than that of the $NiFe_2O_4$/rGO-PVDF electrode, which suggests that the CMC can firmly bond the active materials on the current collector and thus relieve a larger volume change. Furthermore, the electrode morphology is found to be significantly influenced by the binder from the cross-sectional image of the composite electrode during charge/discharge processes, observed by SEM shown in Fig. 8. It is clearly seen that the thickness of the

$NiFe_2O_4$/rGO-CMC electrode hardly changes (Fig. 8a c), whereas, the $NiFe_2O_4$/rGO-PVDF electrode presents a remarkable increase in the thickness after the electrochemical cycling test (50 cycles), as shown in Fig. 8b d, which may be due to the formation of big cracks after cycles, corresponding to the large volume expansion/shrinkage and accumulation of the electrolyte decomposition products at the electrode [49].

Fig. 8

Furthermore, carboxylic groups of carboxymethylcellulose [42] allow facile Li-ion transportation and contribute to form stable SEI film on the surface of the active materials. XPS studies on the $NiFe_2O_4$/rGO-CMC and $NiFe_2O_4$/rGO-PVDF electrodes after 3rd and 50th cycling were investigated (Fig. 9) to reveal that CMC could assist in building a stable SEI film. The surface atomic percentage of the composition was shown in Table 1. For the $NiFe_2O_4$/rGO-CMC electrode, the composition and surface atomic percentage of the SEI layer formed with CMC binder after 50 cycles do not change significantly, obtained from C 1s, F 1s, Li 1s and O 1s core level analysis and Table 1. Accordingly, the surface chemistry of the SEI layer formed with CMC binder does not show great change between the 3rd and 50th cycle, suggesting good SEI stability. However, the SEI layer formed with PVDF binder exhibits considerable variation of the surface atomic percentage after 50 cycles.

Fig. 9

4. Conclusions

In summary, the $NiFe_2O_4$/rGO composites have been successfully synthesized through hydrothermal-annealing method. When evaluated as anode materials for LIBs, the obtained composites electrode with CMC binder display very stable capacity retention of about 1105mAh g^{-1} at a current rate of 100 mA g^{-1} for over 50 cycles. On one hand, the improvement can be attributed to the conductivity network and appropriate proportion of rGO in the $NiFe_2O_4$/rGO composites. On the other hand, the synergic effect on the binder and active materials is very critical in enhancing the performance of spinel metal oxides electrodes. Additionally, CMC as the binder possesses higher adhesion strength, associated with better stability of the electrode and SEI layer during cycling to prevent the pulverization and subsequent decomposition of electrolyte on the $NiFe_2O_4$/rGO surface. As a consequence, the effective and facile strategy to improve the lithium storage performance of $NiFe_2O_4$ provided by this work can be employed to promote the enhancement in the electrochemical performance of spinel metal oxides/sulfides as anodes for LIBs.

Acknowledgments

This work is financially supported by National Nature Science Foundation of China (11674187, 11604172, and 11504192), Shandong Province Natural Science Foundation (ZR2012FZ006 and BS2014CL010), and China Postdoctoral Science Foundation (2014M551868 and 2015M570570). The Taishan Scholar's Program is acknowledged.

Notes and references

[1] J. B. Goodenough, Y. Kim, Challenges for Rechargeable Li Batteries, Chem. Mater., 22 (2010) 587-603.

[2] K. Ding, J. Zhao, J. Zhou, Y. Zhao, Y. Chen, L. Liu, L. Wang, X. He, Z. Guo, A novel material $Li_2NiFe_2O_4$: Preparation and performance as anode of lithium ion battery, Mater. Chem. Phys., 177 (2016) 31-39.

[3] L. Zhang, H. B. Wu, S. Madhavi, H. H. Hng, X. W. Lou, Formation of Fe_2O_3 microboxes with hierarchical shell structures from metal-organic frameworks and their lithium storage properties, J. Am. Chem. Soc., 134 (2012) 17388-17391.

[4] M. Ren, M. Yang, W. Liu, M. Li, L. Su, C. Qiao, X. Wu, H. Ma, Ultra-small Fe_3O_4 nanocrystals decorated on 2D graphene nanosheets with excellent cycling stability as anode materials for lithium ion batteries, Electrochim. Acta, 194 (2016) 219-227.

[5] X. Zhang, Z. Yang, C. Li, A. J. Xie, Y. H. Shen, A novel porous tubular Co_3O_4: Self-assembly and excellent electrochemical performance as anode for lithium-ion batteries, Appl. Surf. Sci., 403 (2017) 294-301.

[6] L. Gu, W. Xie, S. Bai, B. Liu, S. Xue, Q. Li, D. He, Facile fabrication of binder-free NiO electrodes with high rate capacity for lithium-ion batteries, Appl. Surf. Sci., 368 (2016) 298-302.

[7] X. Li, A. Dhanabalan, C. Wang, Enhanced electrochemical performance of porous NiO–Ni nanocomposite anode for lithium ion batteries, J. Power Sources, 196 (2011) 9625-9630.

[8] Y. Zhao, Z. Song, X. Li, Q. Sun, N. Cheng, S. Lawes, X. Sun, Metal organic frameworks for energy storage and conversion, Energy Storage Mater., 2 (2016) 35-62.

[9] C. Liang, M. Gao, H. Pan, Y. Liu, M. Yan, Lithium alloys and metal oxides as high-capacity anode materials for lithium-ion batteries, J. Alloy. Compd., 575 (2013) 246-256.

[10] L. Ouyang, Z. Cao, H. Wang, R. Hu, M. Zhu, Application of dielectric barrier discharge plasma-assisted milling in energy storage materials – A review, J. Alloy. Compd., 691 (2017) 422-435.

[11] X. Guo, X. Lu, X. Fang, Y. Mao, Z. Wang, L. Chen, X. Xu, H. Yang, Y. Liu, Lithium storage in hollow spherical $ZnFe_2O_4$ as anode materials for lithium ion batteries, Electrochem. Commun., 12 (2010) 847-850.

[12] Z. Wang, X. Zhang, Y. Li, Z. Liu, Z. Hao, Synthesis of graphene–$NiFe_2O_4$ nanocomposites and their electrochemical capacitive behavior, J. Mater. Chem. A, 1 (2013) 6393-6399.

[13] J. Wang, G. Yang, L. Wang, W. Yan, Synthesis of one-dimensional $NiFe_2O_4$ nanostructures: tunable morphology and high-performance anode materials for Li ion batteries,J. Mater. Chem. A, 4 (2016) 8620-8629.

[14] L. Luo, R. Cui, K. Liu H. Qiao, Q. Wei, Electrospun preparation and lithium storage properties of $NiFe_2O_4$ nannofibers, Ionics, 21(2015) 687-694.

[15] X. Chen, Y. Huang, K. Zhang, X. Feng, S. Li, Self-assembled flower-like $NiFe_2O_4$ decorated on 2D graphene nanosheets composite and their excellent electrochemical performance as anode materials for LIBs, J. Alloy. Compd., 686 (2016) 905-913.

[16] C. M. Park, J. H. Kim, H. Kim, H. J. Sohn, Li-alloy based anode materials for Li secondary batteries, Chem. Soc. Rev., 39 (2010) 3115-3141.

[17] B. Li, S. Yang, S. Li, B. Wang, J. Liu, From commercial sponge toward 3D graphene-silicon networks forsuperior lithium storage, Adv. Energy Mater., 5 (2015) 1500289-1500295.

[18] P. Zhu, S. Liu, J. Xie, S. Zhang, G. Cao, X. Zhao, Facile synthesis of $NiFe_2O_4$/reduced graphene oxide hybrid with enhanced electrochemical lithium storage performance, J. Mater. Sci.Technol., 30 (2014) 1078-1083.

[19] Y. Ding, Y. Yang, H. Shao, One-pot synthesis of $NiFe_2O_4$/C composite as an anode material for lithium-ion batteries, J. Power Sources, 244 (2013) 610-613.

[20] J. Li, H. M. Dahn, L. J. Krause, D. B. Le, J. R. Dahn, Impact of binder choice on the performance of α-Fe_2O_3 as a negative electrode, J. Electrochem. Soc. 155 (2008) A812-A816.

[21] G. Z. Yang, H. Cui, G. W. Yang, C. X. Wang, Self-assembly of $Co_3V_2O_8$ multilayered nanosheets: controllable synthesis, excellent Li-storage properties, and investigation of electrochemical mechanism, Acs Nano 8 (2014) 4474–4487.

[22] X. Wang, Y. Xiao, J. Q. Wang, L. N. Sun, M. H. Cao, Facile fabrication of molybdenumdioxide/nitrogen-doped graphenehybrid as high performance anode material for lithium ion batteries, J. Power Sources 274 (2015) 142-148.

[23] T. Bansala, S. Mukhopadhyay, M. Joshi, R. Doong, M. Chaudhary, Synthesis and shielding properties of PVP-stabilized-AgNPs-based graphene nanohybrid in the Ku band, Synthetic Met., 221 (2016) 86-94.

[24] Z. Zhang, W. Zhang, D. Li, Y. Sun, Z. Wang, C. Hou, L. Chen, Y. Cao, Y. Liu, Mechanical and anticorrosive properties of graphene/epoxy resin composites coating prepared by in-situ method, Int. J. Mol. Sci., 16 (2015) 2239-2251.

[25] Q. Liu, X. Zhu, Z. Huo, X. He, Y. Liang, M. Xu, Electrochemical detection of dopamine in the presence of ascorbic acid using PVP/graphene modified electrodes, Talanta, 97 (2012) 557-562.

[26] X. Zhi, H. Fang, C. Bao, G. Shen, J. Zhang, K. Wang, S. Guo, T. Wan, D. Cui, The immunotoxicity of graphene oxides and the effect of PVP-coating, Biomater., 34 (2013) 5254-5261.

[27] X. Chang, Z. Wang, S. Quan, Y. Xu, Z. Jiang, L. Shao, Exploring the synergetic effects of graphene oxide (GO) and polyvinylpyrrodione (PVP) on poly(vinylylidenefluoride) (PVDF) ultrafiltration membrane performance, Appl. Surf. Sci., 316 (2014) 537-548.

[28] L. Liu, Synthesis of Fe_2O_3/graphene composite anode materials with good cycle stability for lithium-ionbatteries, Int. J. Electrochem. Sci., (2016) 8654-8661.

[29] W. Xiao, Z. Wang, H. Guo, Y. Zhang, Q. Zhang, L. Gan, A facile PVP-assisted hydrothermal fabrication of Fe_2O_3/Graphene composite as high performance anode material for lithium ion batteries, J. Alloy Compd., 560 (2013) 208-214.

[30] F. Ren, G. Zhu, P. Ren, K. Wang, X. Cui, X. Yan, Cyanate ester resin filled with graphene nanosheets and $CoFe_2O_4$-reduced graphene oxide nanohybrids as a microwave absorber, Appl. Surf. Sci., 351 (2015) 40-47.

[31] L. Liu, L. M. Sun, J. Liu, X. L. Xiao, Z. B. Hu, X. Z. Cao, B. Y. Wang, X. F. Liu, Enhancing the electrochemical properties of $NiFe_2O_4$ anode for lithium ion battery through a simple hydrogenation modification, Int. J. Hydrogen Energ., 39 (2014) 11258-11266.

[32] S. F. Tong, M. B. Zheng, Y. Lu, Z. X. Lin, J. Li, X. P. Zhang, Y. Shi, P. He, H. S. Zhou, Mesoporous NiO with a single-crystalline structure utilized as a noble metal-free catalyst for nonaqueous Li–O_2 batteries, J. Mater. Chem. A, 3 (2015) 16177-16182.

[33] J. Wang, G. Wang, H. Wang, Flexible free-standing Fe_2O_3/graphene/carbon nanotubes hybrid films as anode materials for high performance lithium-ion batteries, Electrochim.Acta, 182 (2015) 192-201.

[34] M. S. Balogun, Y. Luo, W. Qiu, P. Liu, Y. Tong, A review of carbon materials and their composites with alloy metals for sodium ion battery anodes, Carbon, 98 (2016) 162-178.

[35] F. Zhang, D. Jiang, X. Zhang, Porous NiO materials prepared by solid-state thermolysis of a Ni-MOF crystal for lithium-ion battery anode, Nano-Structures & Nano-Objects, 5 (2016) 1-6.

[36] Y. Xiao, J. Zai, X. Li, Y. Gong, B. Li, Q. Han, X. Qian, Polydopamine functionalized graphene/$NiFe_2O_4$ nanocomposite with improving Li storage performances, Nano Energy, 6 (2014) 51-58.

[37] G. Huang, F. Zhang, L. Zhang, X. Du, J. Wang, L. Wang, Hierarchical $NiFe_2O_4/Fe_2O_3$ nanotubes derived from metal organic frameworks for superior lithium ion battery anodes, J. Mater. Chem. A, 2 (2014) 8048.

[38] G. D. Park, J. S. Cho, Y. C. Kang, Multiphase and double-layer $NiFe_2O_4$@NiO-hollow-nanosphere-decorated reduced graphene oxide composite powders prepared by spray pyrolysis applying nanoscale kirkendall diffusion, ACS Appl. Mater. Inter., 7 (2015) 16842-16849.

[39] C. Chen, S. H. Lee, M. Cho, J. Kim, Y. Lee, Cross-linked chitosan as an efficient binder for Si anode of Li-ion batteries, ACS Appl. Mater. Inter., 8 (2016) 2658-2665.

[40] H. Yu, H. S. Fan, B. Yadian, H. T. Tan, W. L. Liu, H. H. Hng, Y. Z. Huang, Q. Y. Yan, General approach for MOF-derived porous spinel AFe_2O_4hollow structures and their superior lithium storage properties, ACS Appl. Mater. Inter., 7 (2015) 26751-26757.

[41] S. Wu, X. Shen, G. Zhu, H. Zhou, Z. Ji, K. Chen, A. Yuan, Synthesis of ternary Ag/ZnO/$ZnFe_2O_4$ porous and hollow nanostructures with enhanced photocatalytic activity, Appl. Catal. B: Environ., 184 (2016) 328-336.

[42] X. Wang, Y. Xiao, C. Hu, M. Cao, A dual strategy for improving lithium storage performance, a case of Fe_2O_3, Mater. Res. Bull., 59 (2014) 162-169.

[43] J. Li, Y. Zhao, N. Wang, Y. Ding, L. Guan, Enhanced performance of a MnO_2–graphene sheet cathode for lithium ion batteries using sodium alginate as a binder, J. Mater. Chem., 22 (2012) 13002-13010.

[44] M. Ling, Y. Xu, H. Zhao, X. Gu, J. Qiu, S. Li, M. Wu, X. Song, C. Yan, G. Liu, S. Zhang, Dual-functional gum arabic binder for silicon anodes in lithium ion batteries, Nano Energy, 12 (2015) 178-185.

[45] Y. Zhao, X. Li, B. Yan, D. Li, S. Lawes, X. Sun, Significant impact of 2D graphene nanosheets on large volume change tin-based anodes in lithium-ion batteries: A review, J. Power Sources, 274 (2015) 869-884.

[46] Y. Z. Qin, Q. Li, J. Xu, X. Wang, G. X. Zhao, C. K. Liu, X. Yan, Y. Z. Long, S. S. Yan, S. D. Li, CoO-Co nanocomposite anode with enhanced electrochemical performance for lithium-ion batteries, Electrochim. Acta, 224 (2017) 90-95.

[47] M. Y. Wu, X. C. Xiao, N. Vukmirovic, S. D. Xun, P. K. Das, X. Y. Song, P. O. Velasco, D. D. Wang, A. Z. Weber, L. W. Wang, V. S. Battaglia, W. L. Yang, G. Liu, Toward an ideal polymer binder design for high-capacity battery anodes, J. Am. Chem. Soc., 135 (2013) 12048-12056.

[48] L. Y. Gong, M. H. T. Nguyen, E. S. Oh, High polar polyacrylonitrile as a potential binder for negative electrodes in lithiumion batteries, Electrochem. Commun., 29 (2013) 45-47.

[49] S. Komaba, N. Yabuuchi, T. Ozeki, Z. J. Han, K. Shimomura, H. Yui, Y. Katayama, T. Miura, Comparative study of sodium polyacrylate and poly-(vinylidene fluoride) as binders for high

capacity Sigraphite composite negative electrodes in Li-ion batteries, J. Phys. Chem. C, 116 (2012) 1380-1389.

Figure caption

Fig. 1 Schematic illustration of the formation mechanism of the $NiFe_2O_4$/rGO composite.

Fig. 2 (a) X-ray diffraction patterns, XPS spectra of the $NiFe_2O_4$/rGO composites: (b) survey, (c) C 1s, (d) Ni 2p, (e) Fe 2p and (f) TGA curves of the $NiFe_2O_4$/rGO composites.

Fig. 3 (a) Raman spectra of the $NiFe_2O_4$, rGO and $NiFe_2O_4$/rGO and (b) N_2 adsorption-desorption isotherms and pore size distributions of the $NiFe_2O_4$/rGO composites.

Fig. 4 Low and high-magnification FE-SEM images of the as-synthesized $NiFe_2O_4$/rGO composites.

Fig. 5 The tapping mode AFM images and height images of GO (a and b) and $NiFe_2O_4$/rGO (c and d) nanoplatelets deposited on a silicon surface by the ultrasonic treatment in DI water.

Fig. 6 (a) Representative cyclic voltammograms (CVs) at a scan rate of 0.2 mV s^{-1} between 0.01 and 3 V *vs.* Li/Li^+, (b) Charge-discharge voltage profiles of the $NiFe_2O_4$/rGO composites for the 1st, 2nd, 10th and 50th cycles at a current rate of 100 mAg^{-1}, (c) Cycling performance of the A (50 mg rGO), B (100 mg rGO), C (150 mg rGO) and D (0 mg rGO) composites with CMC and PVDF, respectively, at a current rate of 100 mA g^{-1}, and (d) Capacity and Coulombic efficiency *vs.* Cycle number of the B composite with CMC at a current rate of 1 A g^{-1}.

Fig. 7 (a) Rate capability of the A composite with CMC, B composite with CMC and B composite with PVDF, (b) Nyquist plots of B sample with CMC and PVDF in the fresh

and cycle state and inset: the equivalent electrical circuit, (c) An adhesion strength test of $NiFe_2O_4$/rGO-PVDF and (d) An adhesion strength test of $NiFe_2O_4$/rGO-CMC.

Fig. 8 Cross-sectional SEM images (BEI mode) of the $NiFe_2O_4$/rGO-CMC (a, c) and $NiFe_2O_4$/rGO-PVDF electrodes (b, d): (a, b) after 3rd electrodes and (c, d) after 50 cycles.

Fig. 9 (a) C 1s, (b) F 1s, (c) Li 1s and (d) O 1s XPS spectra on the anode surface after the 3rd and 50th cycle of the $NiFe_2O_4$/rGO-CMC electrode.

Figr-1

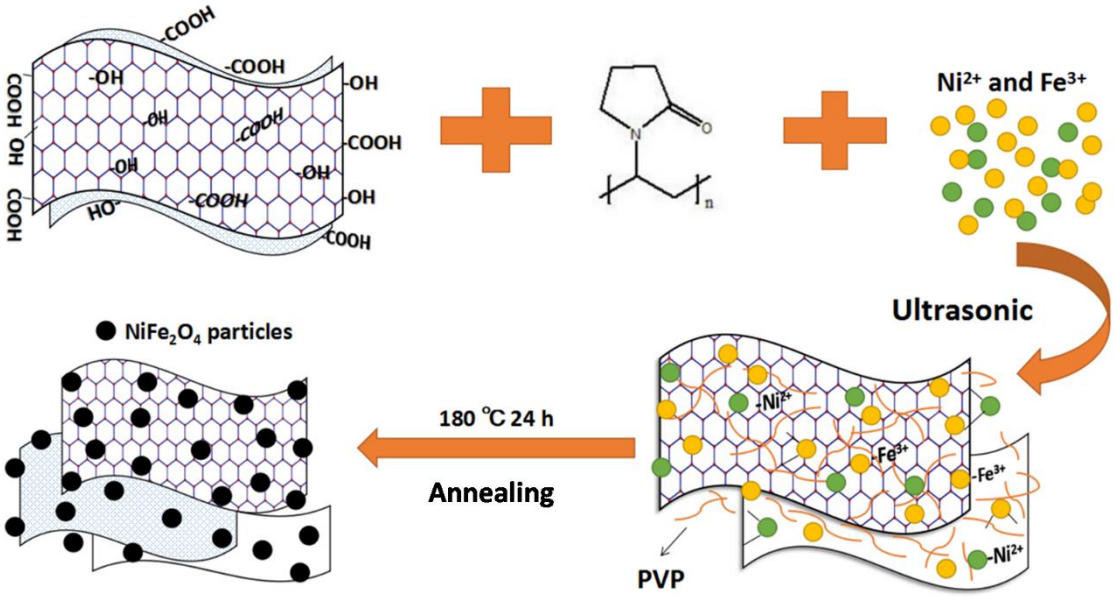
-COOH
-COOH
-OH
-OH
COOH OH COOH
-OH
-COOH
-COOH
-OH
-OH
-OH
HO-
-COOH
-OH
-COOH
N
O
n
Ni²⁺ and Fe³⁺
Ultrasonic
NiFe₂O₄ particles
180 °C 24 h
Annealing
-Ni²⁺
-Fe³⁺
-Fe³⁺
-Ni²⁺
PVP

Figr-2

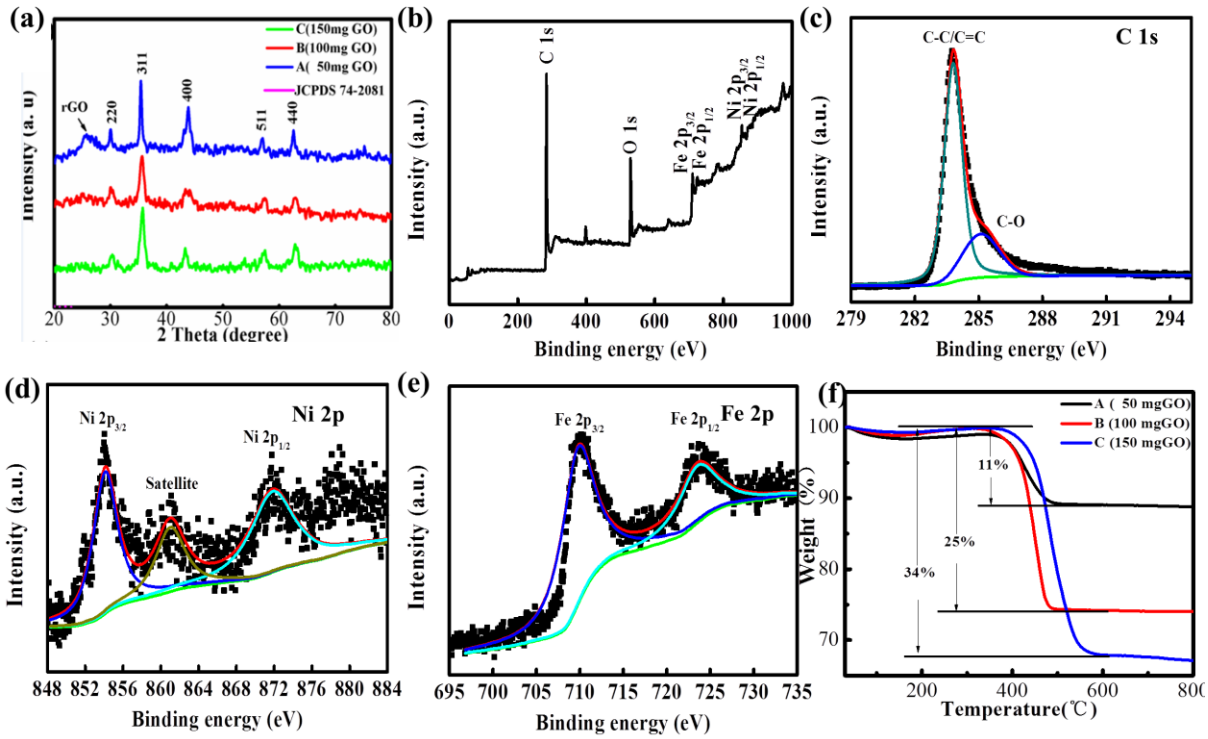

Figr-3

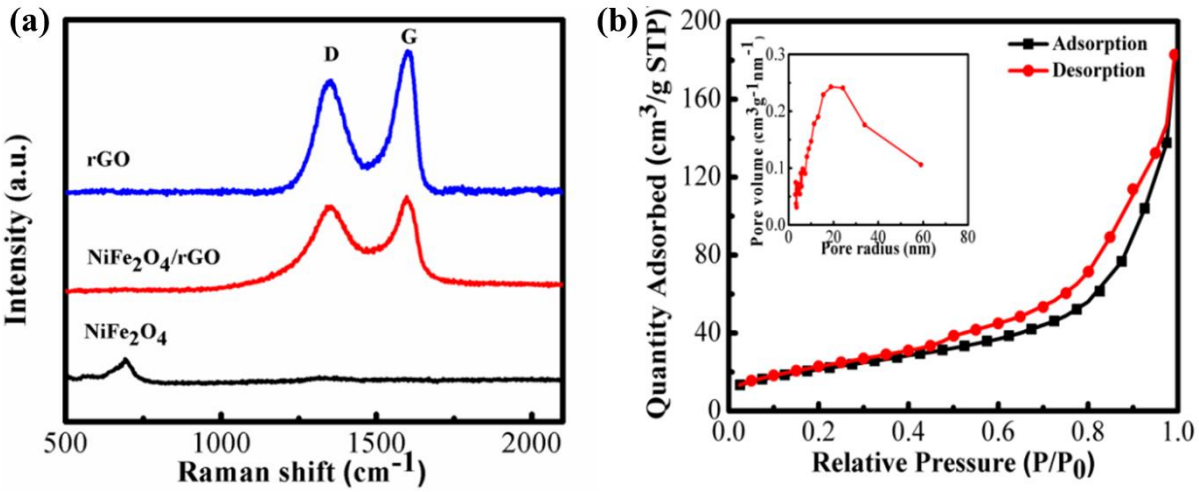

Figr-4

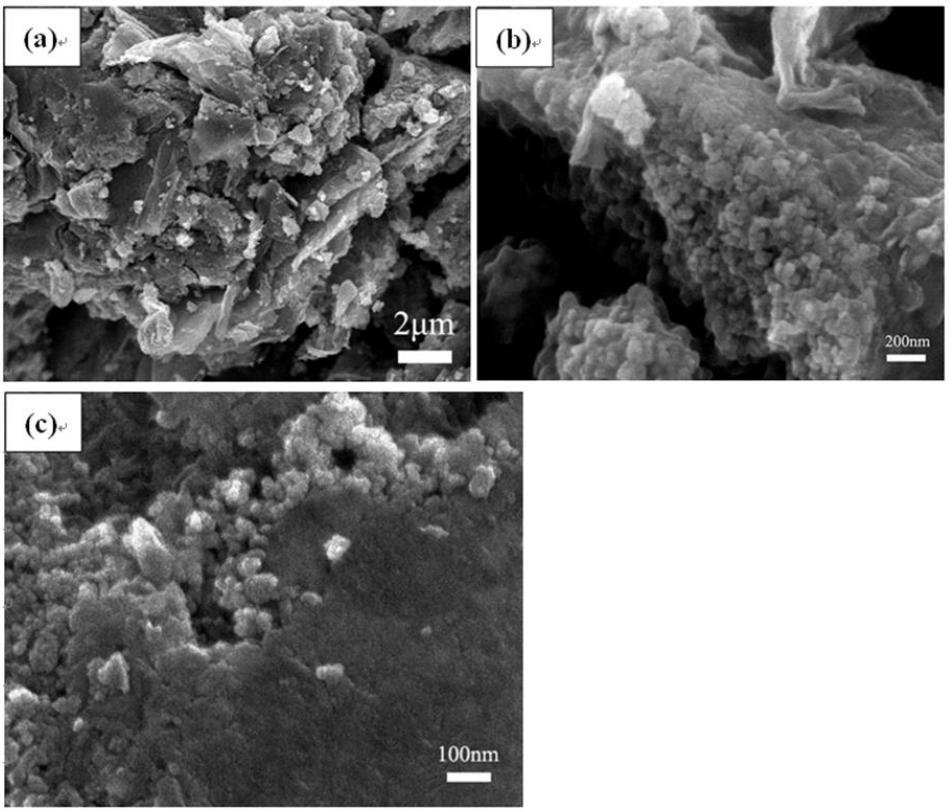

Figr-5

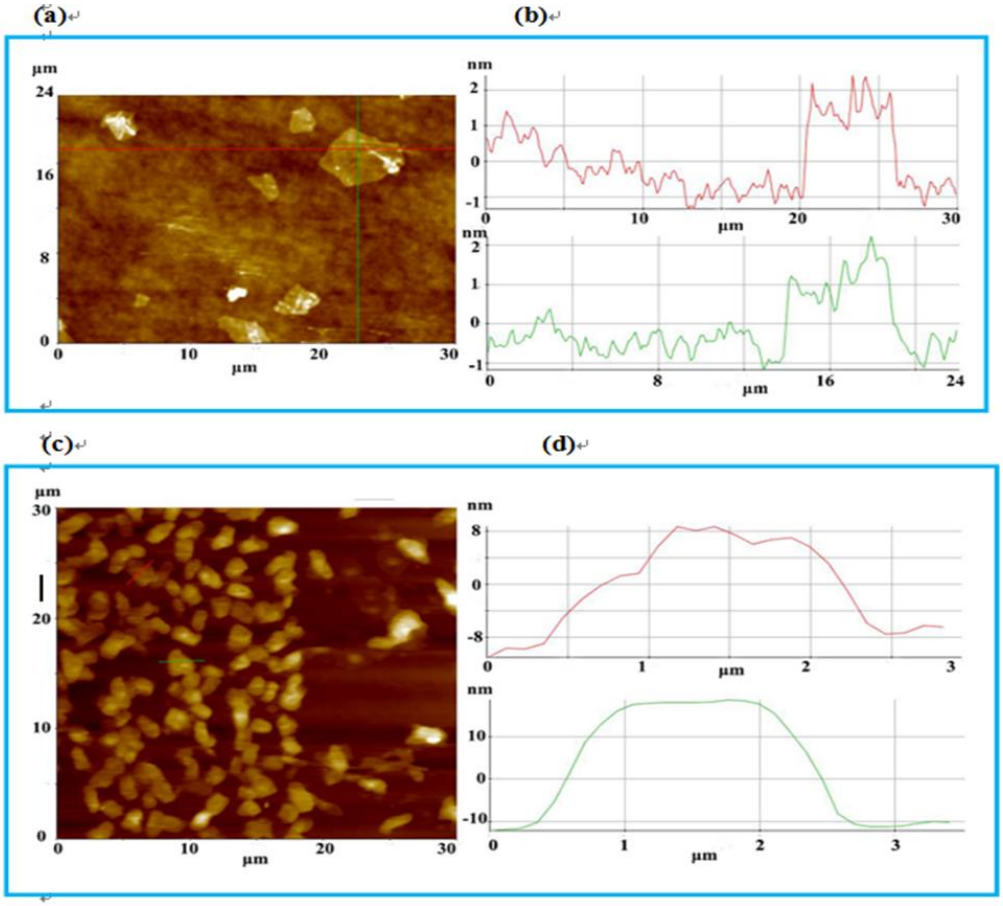

Figr-6

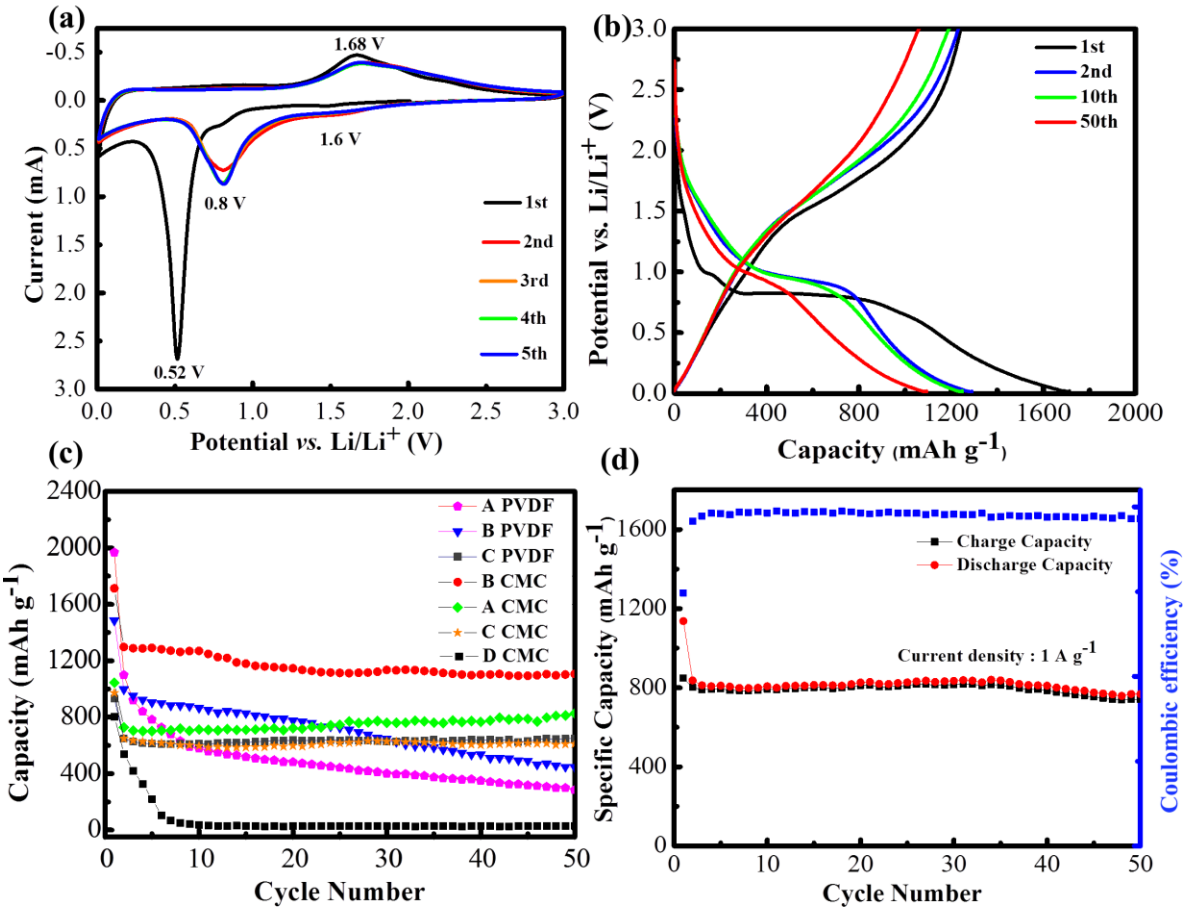

Figr-7

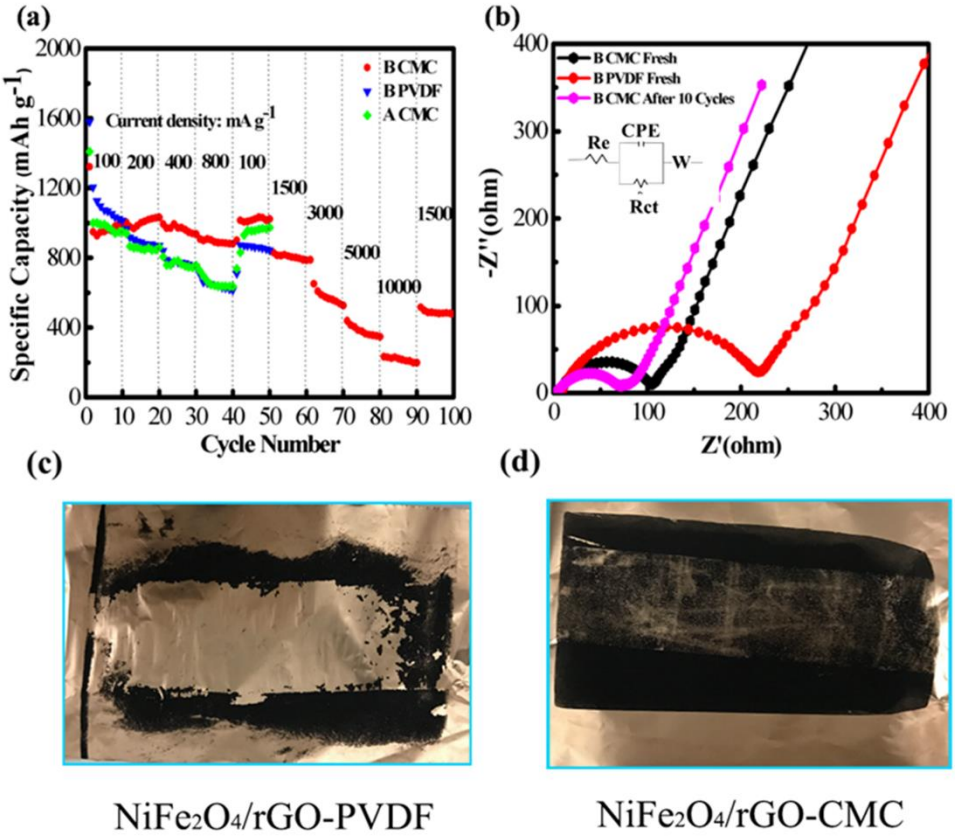

$NiFe_2O_4$/rGO-PVDF

$NiFe_2O_4$/rGO-CMC

Figr-8

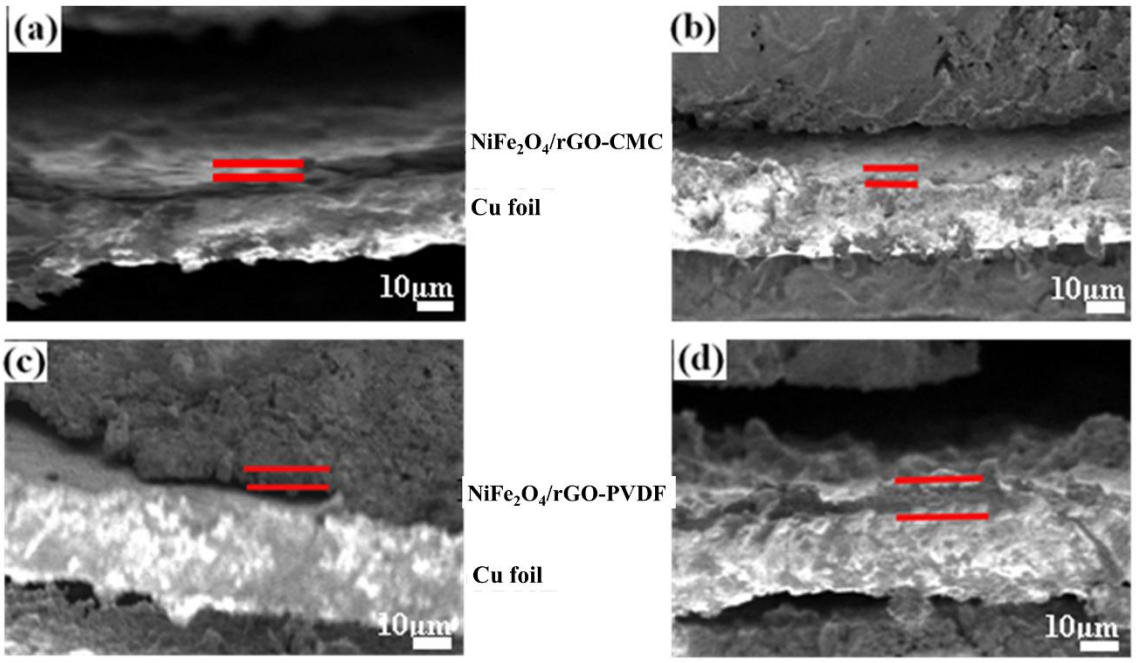

Figr-9

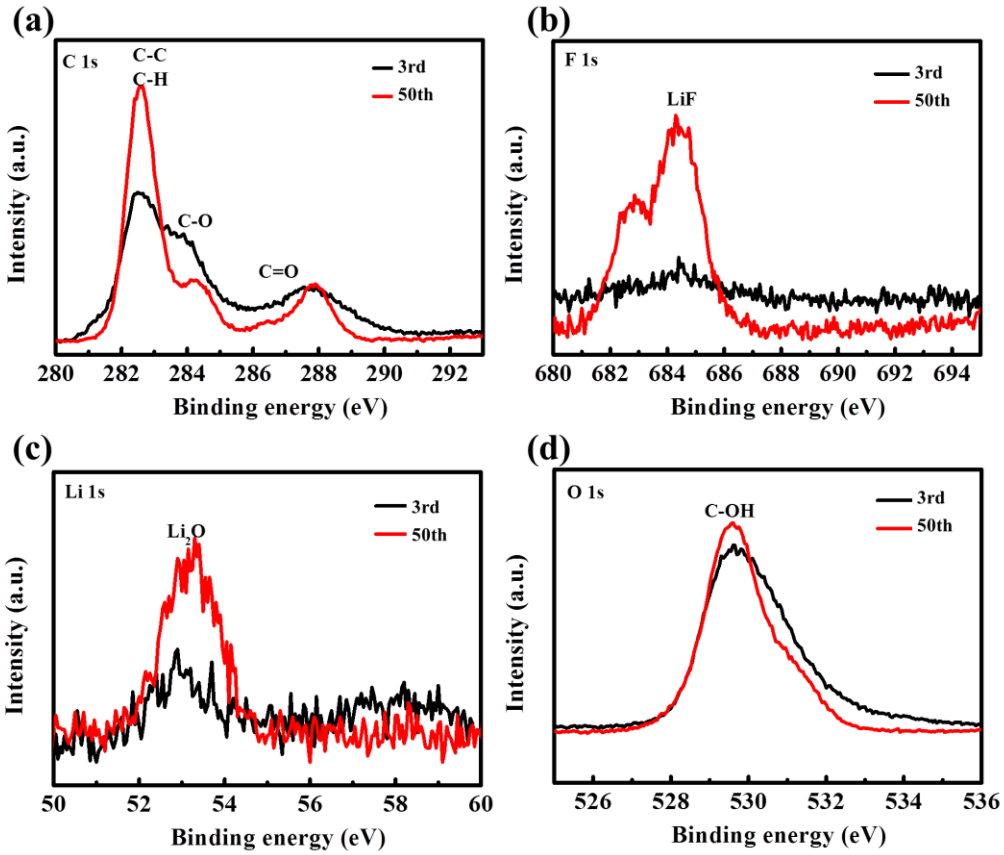

Table 1 Surface composition (atomic percentage) for 3rd and 50th cycled $NiFe_2O_4$/rGO-CMC and $NiFe_2O_4$/rGO-PVDF electrodes measured by XPS.

Atom		C	O	F	Li	P
Atom percentage (%)	CMC-3rd	54.55	29.11	1.62	14.36	0.37
	CMC-50th	53.86	27.85	5.64	11.77	0.87
	PVDF-3rd	37.80	23.47	17.24	19.91	1.58
	PVDF-50th	38.70	31.31	2.29	27.30	0.41